Ultrasound in Med. & Biol., Vol. 31, No. 9, pp. 1143–1158, 2005

0301-5629/05/$–see front matter

ELSEVIER

doi:10.1016/j.ultrasmedbio.2005.03.016

● *Original Contribution*

SEGMENTATION OF REAL-TIME THREE-DIMENSIONAL ULTRASOUND FOR QUANTIFICATION OF VENTRICULAR FUNCTION: A CLINICAL STUDY ON RIGHT AND LEFT VENTRICLES

ELSA D. ANGELINI,* SHUNICHI HOMMA,† GREGORY PEARSON,‡ JEFFREY W. HOLMES,§ and ANDREW F. LAINE§

*Ecole Nationale Supérieure des Télécommunications, Paris, France; †Department of Medicine, Columbia University, New York, NY, USA; ‡College of Physicians & Surgeons, Columbia University, New York, NY, USA; and §Department of Biomedical Engineering, Columbia University, New York, NY, USA

(*Received* 28 *July* 2004, *revised* 14 *March* 2005, *in final form* 22 *March* 2005)

Abstract—Among screening modalities, echocardiography is the fastest, least expensive and least invasive method for imaging the heart. A new generation of three-dimensional (3-D) ultrasound (US) technology has been developed with real-time 3-D (RT3-D) matrix phased-array transducers. These transducers allow interactive 3-D visualization of cardiac anatomy and fast ventricular volume estimation without tomographic interpolation as required with earlier 3-D US acquisition systems. However, real-time acquisition speed is performed at the cost of decreasing spatial resolution, leading to echocardiographic data with poor definition of anatomical structures and high levels of speckle noise. The poor quality of the US signal has limited the acceptance of RT3-D US technology in clinical practice, despite the wealth of information acquired by this system, far greater than with any other existing echocardiography screening modality. We present, in this work, a clinical study for segmentation of right and left ventricular volumes using RT3-D US. A preprocessing of the volumetric data sets was performed using spatiotemporal brushlet denoising, as presented in previous articles Two deformable-model segmentation methods were implemented in 2-D using a parametric formulation and in 3-D using an implicit formulation with a level set implementation for extraction of endocardial surfaces on denoised RT3-D US data. A complete and rigorous validation of the segmentation methods was carried out for quantification of left and right ventricular volumes and ejection fraction, including comparison of measurements with cardiac magnetic resonance imaging as the reference. Results for volume and ejection fraction measurements report good performance of quantification of cardiac function on RT3-D data compared with magnetic resonance imaging with better performance of semiautomatic segmentation methods than with manual tracing on the US data. (laine@columbia.edu)

Key Words: **Segmentation, Echocardiography, RT3-D, 3-D ultrasound, Level set, Denoising, Clinical study, LV, RV, Pulmonary hypertension.**

INTRODUCTION AND LITERATURE

A reliable noninvasive imaging modality is essential for evaluating and monitoring patients with cardiac disease. Traditional screening techniques for quantitative assessment of cardiac function include multigated angiography (MUGA), magnetic resonance imaging (MRI), computerized tomography (CT), nuclear imaging and ultrasound (US). Among these modalities, US is the fastest, least expensive and least invasive screening modality for imaging the heart. Because of the 3-D structure and deformation of the heart muscle during the cardiac cycle, analysis of irregularly shaped cardiac chambers or description of valve morphology using 2-D images is inherently limited. Developments in 3-D echocardiography started in the late 1980s with the introduction of offline 3-D medical US imaging systems. Many review articles have been published over the past decade, assessing the progress and limitations of 3-D US technology for clinical screening (Belohlavek et al. 1993; Fenster and Downey 2000; Ofili and Nanda 1994; Rankin et al. 1993). These articles reflect the diversity of 3-D systems that were developed for both image acquisition and reconstruction, developed in three generations: 1. freehand

Address correspondence to: Andrew F. Laine, D.Sc, Department of Biomedical Engineering, Columbia University, 416 CEPSR, MC8904, 530 West 120th street, New York, NY 10027 USA. E-mail: laine@columbia.edu

scanning that acquires planar views at arbitrary spatial positions and orientation with a 2-D transducer; 2. mechanical scanning that acquires planar views with a 2-D transducer moved at regular intervals along a specified path; and 3. matrix phased-array transducers that scan a true three-dimensional volume at each pulse, as introduced by Von Ramm and Smith (1990). This technology, pioneered by Von Ramm at Duke University with the Volumetrics© transducer, was fundamentally different from the former generations of 3-D systems, as the entire cardiac volume was acquired in real-time (one scan for one cardiac cycle), enabling the cardiologist to view moving cardiac structures from any given plane over a single cardiac cycle (Kisslo et al. 2000; Morsy et al. 1997; Ota et al. 1990; Shattuck et al. 1984; Shiota et al. 1998; Stetten et al. 1998). Direction of pulse transmission and acquisition is controlled by individual transducer elements. With a linear 1-D array, the transducer controls the direction within a slice in 3-D space, referred to as the azimuth. With this 2-D matrix array, the steering is controlled in both the azimuth and the elevation directions, allowing the acquisition of an entire pyramidal shape. Samples are acquired slice by slice at evenly spaced depths. The spacing between each scanning depth is equal to 0.308 mm in radial coordinates. This spacing determines the resolution in the receive line direction. A maximum of 512 slices can be acquired with the transducer. The RT3-D transducer array operates at frequencies between 2.0 MHz and 3.5 MHz. The particular design of the transmitter and receiver lines achieves a 16:1 parallel processing mode, allowing extremely fast acquisition. For a depth setting of 6 cm, the transducer can reach a scan rate of 40 volumes per second and for a setting of 20 cm, the scan rate reaches 14 volumes per second. Typical transthoracic cardiac screenings are performed by placing the transducer at the apex location and scanning a volume through 15–20 cm depth, acquiring between 15 and 20 volumes per cardiac cycle. The transducer produces 8-bit data matrices of size $64 \times 64 \times 512$ every 1/22 s, which corresponds to 46 Mbytes of data per s. More recently, Philips Medical Systems (Andover, MA, USA) introduced the first generation (SONOS 7500) and second generation (iE33) matrix-phased array RT3-D US systems.

Since all volumes are acquired in seconds with a single scan, the task of the clinician is reduced simply to positioning the heart within the scanners' field-of-view (FOV). No cardiac or respiratory gating is required during the acquisition and no postprocessing is necessary for tomographic reconstruction, as was the case with early 3-D US technology. From a quantitative perspective, continuous direct measurement of cardiac volumes and myocardium wall deformation without geometrical assumptions are made possible. In a recent review, Fenster et al. (2001) stated that, although 3-D US technology has been developed for over a decade, it is only now achieving widespread use with numerous clinical applications. Improvements in reconstruction algorithms, display techniques and computer power account for the increasing interest and confidence from the clinical community. Nevertheless, full exploitation of 3-D US data for qualitative and quantitative evaluation of cardiac function remains suboptimal because of lack of automatic boundary detection. Currently, 2-D slices extracted from a 3-D volume data set are manually traced to determine ventricular volumes and quantify cardiac function. This tedious task requires the intervention of an expert cardiologist familiar with the US machine. For this reason, ventricular volumes are commonly estimated *via* visual inspection of B-scan images. Manual segmentation is only performed in difficult cases for which an "objective" measure is required. An automated segmentation process or one with minimal manual intervention would provide a more accurate method to calculate chamber volumes, with a significant saving of time.

Segmentation of cardiac US has drawn a lot of attention in the medical imaging community and is still an active research area. The main challenges for segmentation of US images lie in the poor quality of the signal due to low spatial resolution of the hardware system, attenuation and motion artefacts that lead to ill-defined myocardial borders and addition of frequency-dependent speckle noise that corrupts the specificity of grey-level values to characterize the presence of an interface or a particular tissue type. Several approaches have been reported during the past two decades for epicardial and endocardial border detection from US data with partial success. For high-resolution 2-D B-mode US, simple segmentation techniques using matched filtering (Detmer et al. 1990) and morphological filters (Klingler et al. 1988; Thomas et al. 1991) reported good performance. Recent studies include more elaborated algorithms that can be divided into region classifiers and deformable model methods.

1. Segmentation methods based on region classifiers rely on the representation of an image in terms of homogeneous areas. Statistical classifiers derive data or object likelihood based on local intensity statistical measures. The most popular statistical segmentation framework is derived from Bayesian statistics with maximum *a posteriori* estimation of the object to segment *via* classification into separate classes corresponding to homogeneous regions of different tissue types (Ashton and Parker 1995; Dias and Leitao 1996; Drezek et al. 1997; Kao et al. 1998; Morsy et al. 1997; Papadopoulos and Strintzis 1995). Bayesian classifiers require prior statistical models for the observation

signal and individual class distributions. These prior models can be derived from Markov random fields (Ashton and Parker 1995; Boukerroui et al. 1999; Dias and Leitao 1996; Friedland and Adam 1989; Herlin et al. 1994; Herlin and Giraudon 1993; Papadopoulos and Strintzis 1995; Xiao et al. 2002), mixed Rayleigh–Gaussian distributions (Trobaugh and Arthur 2001), fuzzy reasoning (Feng et al. 1991; Setarehdan and Soraghan 1999), artificial neural networks classifiers (Hunter et al. 1995; Xin et al. 1992) and simulated annealing (Friedland and Adam 1989).

2. Deformable models, also referred to as active contours, have been successfully applied to segmentation of US images in cardiac applications for the past two decades (Chalana et al. 1996; Coppini et al. 1995; Drezek et al. 1997; Malassiotis and Strintzis 1999; Mikic et al. 1998; Staib and Duncan 1989). Initially introduced as "snakes" by Kass et al. (1987), this technique performs segmentation of a particular object by deforming a set of points under internal and external forces, respectively, derived from intrinsic mechanical properties of the model and edge information of an underlying image. Deformable models are very efficient at segmenting high-resolution 2-D images with a simple mathematical framework. Limitations arise when applying the technique to noisy US images for the extraction of edge information defining external forces (Chalana et al. 1996; Drezek et al. 1997; Malassiotis and Strintzis 1999; Mikic et al. 1998; Staib and Duncan (1989). General approaches for segmentation of cardiac ultrasound have relied on smoothed gradient maps and optical flows (Mikic et al. 1998). The major limitation of the deformable model segmentation technique deals with its extension to higher dimensions for segmentation of 3-D data sets. Initial efforts were made to extend the parametric formulation to 3-D using elaborated mesh structures, as reviewed in Metaxas (1997) and Montagnat et al. (2001). These deformable models are extremely difficult to implement and manipulate while ensuring, at the same time, stability and adaptivity of the mesh as it deforms (Cohen and Cohen 1993; Jones and Metaxas 1997; Lotjonen et al. 1998; Montagnat et al. 2000). A solution of this problem is to embed the deformable model into a level set framework with an implicit formulation that extends naturally to three and higher dimensions, as proposed by Sethian (1996). This implementation has been tried for cardiac US segmentation in two recent studies by Chen et al. (2003) and Paragios (2003), with only preliminary results and no validation. In a third study by Lin et al. (2003), a level-set deformable model was applied for LV endocardial border detection on 24 2-D images acquired with a rotational 3-D US probe on four patients. LV contours were also defined by three "experienced observers" and results were compared through mean absolute distance. The authors concluded that level set segmentation was in the variation range of manual tracing. Finally, Corsi et al. (2001, 2002) proposed a gradient-based 3-D level set deformable model for RT3-D volume data that relies on edge information. Because of the strong inhomogeneities in the data corrupted by speckle noise, they need to manually initialize the model close to the endocardial borders. They tested their algorithms on a data set on 20 patients, comparing LV volume measurements from their method and from manual tracing on MRI. A detailed comparison of the results reported by their study and ours is provided in the Discussion section of this paper.

In this research project, we have experimented with both parametric and implicit formulations of deformable models for segmentation of the ventricular cavities on RT3-D US. We initially implemented a 2-D deformable model into an explicit parametric formulation, presented in Angelini et al. (2001). We present, in this paper, results with a 3-D implicit formulation of the deformable model.

MATERIALS AND METHODS

Denoising

Ultrasound beams propagate through biological tissue while undergoing distortions due to local inhomogeneities of acoustic parameters and nonlinearity in medium composition. In addition, speckle noise components are introduced during the acquisition process, resulting from constructive and destructive echo signal interferences from random locations. This noise component affects the contrast and resolution of the acquired signal, introducing granular patterns across the images. To improve image quality and remove speckle noise components, US denoising is commonly applied before processing and display.

We approached the denoising problem as a texture characterization task. Because textural patterns are best described by their frequency content and orientation, we investigated an analysis method based on multiscale expansion of the data with brushlet functions, first introduced by Meyer and Coifman (1997) for compression of highly textured images, applied to the Fourier transform of a signal. This work was previously published in Angelini et al. (2001) and Angelini and Laine (2001), with qualitative and quantitative evaluation of denoising quality, comparing brushlet expansion and Wiener filtering.

Denoising performance on clinical RT3-D data is illustrated for spatial and temporal brushlet denoising with optimized parameters in Fig. 1. Overall, our previ-

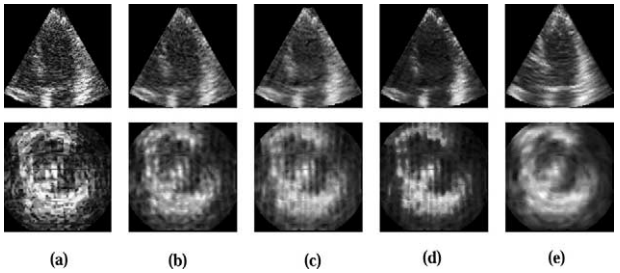

Fig. 1. Qualitative comparison of denoising and enhancement performance on RT3-D clinical data. Denoising results are presented for one long-axis and one short-axis view from a single clinical data set. (a) Original data. (b) Spatial denoising *via* 3-D brushlet. (c) Further temporal denoising *via* 2-D+T frequency brushlet analysis, and (d) *via* 1-D time brushlet analysis. (e) Wiener denoising optimized for speckle noise.

ous studies have shown that denoised RT3-D US performs better than traditional Wiener filtering, providing increased contrast, homogeneous myocardial texture and better definition of myocardium borders at the epicardial and endocardial walls, without smoothing artefacts.

Segmentation with level-set deformable models

Level-set algorithms were introduced by Osher and Sethian (1988) for deformation of moving fronts with curvature-dependent speed. They offer a very simple framework for implementation of deformable surfaces in *n*-D with embedding of the problem into a higher-dimension functional defined with negative, positive and zero levels corresponding, respectively, to the inside, outside and the surface itself (Sethian 1999). Application of level-set methods for segmentation of medical images was first introduced by Malladi et al. (1995). Extensive literature has reported successful implementation of level-set algorithms for multidimensional segmentation of medical images (Chen et al. 2001; Corsi et al. 2001; Kimmel et al. 2000; Loncaric et al. 2000; Malladi et al. 1996; Malladi and Sethian 1996; Sarti et al. 2002; Suri 2000; Wang and Wee 1999; Xiaolan et al. 1999). Because the classical level-set segmentation framework is based on edge information, the medical applications commonly focused on segmentation of high-resolution image modalities, such as MRI and CT. Parallel efforts have been carried out based on the Mumford–Shah functional (Mumford and Shah 1985) to develop region-based deformable models *via* energy minimization into a level-set framework (Chan and Vese 2001; Tsai et al. 2001; Yezzi et al. 1997). This curve-based evolutionary process segments an image by partitioning the data into smooth areas. These methods have shown great potential for segmentation of medical images with low-contrast multiple objects and high curvature contours (Chan and Vese 2001; Tsai et al. 2001; Yezzi et al. 1997). Geodesic active contours from Paragios and Deriche (2000) were introduced recently as a new segmentation framework that unifies the boundary-based and region-based energy minimization approaches with level-set implementation.

Homogeneity-based active contour. We previously experimented with segmentation of RT3-D US with a 2-D parametric deformable model, as presented in Angelini et al. (2001). Extension of parametric formulation to 3-D is very difficult, which led us to investigate an alternative formulation of the deformable model in an implicit level-set framework. Because of the low resolution of RT3-D US data and the poor definition of the myocardial wall, we found that the boundary-based methods were more appropriate for our application, following the work of Chan and Vese (2001) for developing active contours without edges. The proposed method is similar to the segmentation with a deformable model into a two-phased image, combining the following advantages: arbitrary initialization of the object anywhere in the image, no need for gradient information and self adaptation for inward and outward local motion.

Assume that the image $I(x, y)$, defined on the domain Ω, is composed of two homogeneous regions of distinct values I_0 and I_1 and that the object to detect corresponds to the region of intensity I_0. We denote the boundary of the object with intensity I_0 by C_0. For a given curve C of the domain of Ω, we consider the following energy functional $E(C)$:

$$E(C) = E_0(C) + E_1(C) = \int_{inside(C)} |I - c_0|^2 d\Omega + \int_{outside(C)} |I - c_1|^2 d\Omega, \quad (1)$$

where c_0 and c_1 are equal to the average value of I inside and outside C.

The minimum of this energy is achieved for $C = C_0$, when the two terms tend to zero:

$$\min_c(E(C)) = E(C_0) \simeq 0 \quad (2)$$

We see that eqn (1) defines a framework for segmentation of the object C_0 *via* minimization of the energy functional. Similarly to the deformable-model functional, it is desirable to introduce some regularizing terms corresponding to the length $L(C)$ of the curve and the area $A(C)$ of the object enclosed by the curve:

$$E(C) = \mu L(C) + \nu A(C) + \lambda_0 \int_{inside(C)} |I - c_0|^2 d\Omega + \lambda_1 \int_{outside(C)} |I - c_1|^2 d\Omega, \quad (3)$$

where μ, ν, λ_0, λ_1 are fixed positive parameters.

Such regularization *via* penalty on the curve length and area has been applied in many partial-differential-based segmentation methods (Amadieu et al. 1999; Cremers et al. 2001). We note that, in N dimensions, C represents a hypersurface in $\mathbb{R}^N$, $L(C)$ represents the $(N-1)$ Hausdorff dimensional and $A(C)$ represents the Lebesgue measure in $\mathbb{R}^N$. The functional defined in eqn (3) corresponds to a special case of the more general Mumford–Shah functional for approximating the image $I(x, y)$ as a piecewise smooth image $J(x, y)$ and a set of smooth contours C, *via* minimization of the following energy functional:

$$E_{MS}(J, C) = \mu L(C) + \lambda \int_{\Omega} |I - J|^2 d\Omega + \int_{\Omega \setminus C} |\nabla I|^2 d\Omega, \tag{4}$$

where μ and λ are positive parameters. As pointed out by Mumford and Shah (1985), the minimization of the functional in eqn (4) reduces to the minimal partition problem if we restrict the admissible solution population to piecewise constant functions. J, for which $J = \bigcup_i J_i$ and $J_{j_i} = c_i$ with constant values c_i. The solution to this problem identifies the edges of the homogeneous regions in C and the constants c_i are equal to the average of I inside the regions J_i.

Level-set implementation

Let C be a curve defined on $\Omega \subset \mathbb{R}^N$. The level-set framework embeds the curve C in a Lipschitz scalar function ϕ defined on $\mathbb{R}^N$, such that:

$$C = \{x \in \mathbb{R}^N / \phi(x) = 0\} \tag{5a}$$

$$C_{inside} = \{x \in \mathbb{R}^N / \phi(x) < 0\} \tag{5b}$$

$$C_{outside} = \{x \in \mathbb{R}^N / \phi(x) > 0\}. \tag{5c}$$

We see here that the curve C corresponds to the zero-level of the function ϕ on the domain Ω. The level-set implementation of the functional defined in eqn (3) replaces the curve C by the function ϕ and solves the minimization problem for this function. The curve corresponding to the final solution ϕ_0 corresponds to the zero level of this function.

We now define a Heaviside function H as:

$$H(z) = \begin{cases} 1 \text{ if } z \leq 0 \\ 0 \text{ if } z \geq 0 \end{cases}, \tag{6}$$

and the associated Dirac function as:

$$\delta(z) = \frac{dH(z)}{dz}. \tag{7}$$

These functions are used to define the interior and the contour curve C and transpose constraints on the length and area of the curve to integrals over the entire domain Ω. Indeed, based on the Heaviside function, we can approximate the length of the curve C as:

$$L(\phi = 0) = \int_{\Omega} |\nabla H(\phi)| d\Omega = \int_{\Omega} \delta(\phi) |\nabla(\phi)| d\Omega, \tag{8}$$

and the area of the inside of the object to segment as:

$$A(\phi \leq 0) = \int_{\Omega} |H(\phi)| d\Omega. \tag{9}$$

We can then rewrite the energy functional as a function of $H(\phi)$ as:

$$E(C) = \mu L(\phi = 0) + \nu A(\phi \leq 0) + \lambda_0 \int_{\Omega} |I - c_0|^2 H(\phi) d\Omega + \lambda_1 \int_{\Omega} |I - c_1|^2 (1 - H(\phi)) d\Omega. \tag{10}$$

We observe here that the solution that minimizes eqn (3) in the case of the two-values solution can be written as:

$$J = c_0 H(\phi) + c_1 (1 - H(\phi)). \tag{11}$$

The two constants c_0 and c_1 can be expressed in terms of $H(\phi)$ as:

$$c_0 = \frac{\int_{\Omega} I \cdot H(\phi) d\Omega}{\int_{\Omega} H(\phi)}, \quad c_1 = \frac{\int_{\Omega} I \cdot (1 - H(\phi)) d\Omega}{\int_{\Omega} (1 - H(\phi)) d\Omega}, \tag{12}$$

assuming that the function $H(\phi)$ is not constant (*i.e.,* the object to segment is not empty).

This explicit representation of the two constant values transforms the minimization of the energy in eqn (10) to a problem with a single variable $H(\phi)$. The existence of a minimum is ensured by the more general minimal partition problem, whose minimum existence has been proved by Morel and Solimini (1994). Details on the discretization of the minimization problem and the numerical schemes used in this work are reported in the Appendix. A detailed description of the segmentation algorithm is also provided in Angelini et al. (2003). Parameter values used in our implementation were the following. We set $\upsilon = 0$ to eliminate the constant term in eqn (13), which was derived from the area term in eqn (3). This term can be seen as an advection term that should be turned on only if we want to push the model in a constant direction (outward or inward). Here, we wanted the model to be able to move in any direction, allowing more arbitrary position in the initialization. We also set $\lambda_1 = 0$, so that we are not looking for a dual segmentation of the myocardium and the ventricular

cavity as two homogeneous areas but, rather, for a single segmentation of the cavity. The myocardium tissue is rather inhomogeneous and the average intensity term $c_1(\phi)$ associated with this parameter led to unstable behavior of the model when not set to zero. Because the level-set framework allows for topological changes, we forced the segmentation to return a single ventricular cavity by tracking only the closed curve, defined by the level zero of the ϕ function and centered around the center of mass of the initial object. The other parameters were set experimentally to $\lambda_0 = 0.25$, $\mu = 1$ and $\varepsilon = 2$. Spacing steps were set to $\Delta x = \Delta y = \Delta z = 1$. The parameter ε was set to $\varepsilon = 2$. Finally, the time step was constrained to $\Delta t < \frac{\min(\Delta x, \Delta y, \Delta z)}{(|\mu| + |\nu| + |\lambda_0 + \lambda_1|)}$, to ensure stability of the numerical scheme *via* Courant-Friedrichs-Lewy (CFL) condition, and we chose $\Delta t = 0.1$. These parameters values were fixed for all the experiments presented in this paper. Typically, parameters of the energy functional need to be modified if new smoothness constraints are needed or if data sets with different visual quality are used. Volumetrics data sets from the same transducer and acquired with a similar field-of-view can be segmented with a common set of parameters. The stopping criterion, based on the stability of the zero level interface, was defined as in Chan and Vese (2001).

Principal steps of the segmentation algorithm

Segmentation of the US volume data is performed *via* minimization of the energy functional defined in eqn (3). Minimization of the functional *via* steepest gradient descent on a discrete spatial grid indexed with $(i, j, k) \in \mathbb{R}^3$ and introduction of a temporal index (n) leads to an iterative scheme with the following equation of evolution of the level set function:

$$\phi_{i,j,k}^{n+1} = \phi_{i,j,k}^{n} + \Delta t * \delta_{\varepsilon}\left(\phi_{i,j,k}^{n}\right)\Bigg[-\mu Force_{curvature}\left(\phi_{i,j,k}^{n}\right) + \nu + \lambda_0 \frac{\left(I_{i,j,k} - c_0(\phi^n)\right)^2}{c_0(\phi^n)^2} - \lambda_1 \frac{\left(I_{i,j,k} - c_1(\phi^n)\right)^2}{c_1(\phi^n)^2}\Bigg]. \quad (13)$$

The sequence of function ϕ^n for $n \geq 0$ is constructed as follows:

- Start with $n = 0$. Initialize with a set of points a curve C_0 in the image domain. Define ϕ^0 as the signed distance function with zero-level defined at the location of the curve C_0.
- Compute $c_0(\phi^n)$ and $c_1(\phi^n)$ as the average of the function ϕ^n on the domains defined by $\phi^n < 0$ and $\phi^n > 0$, respectively
- Compute the curvature term for ϕ^n with eqn (22) (cf. Appendix)
- Solve eqn (13) to obtain ϕ^{n+1}
- Check whether the solution is stationary; iterate for $n = n + 1$ if not
- The final zero-level is computed as the isosurface of the volume function ϕ^n at level zero.

EXPERIMENTS

We present in this section results for *in vivo* studies performed to validate our method for quantification of ventricular function using RT3-D US.

A clinical study was performed for quantification of right and left ventricular function in patients diagnosed with pulmonary hypertension (PH). This condition results in narrowing of the pulmonary blood vessels that leads to increased pressure in the right ventricle and, eventually to heart failure. Pulmonary hypertension is either primary with unknown cause or secondary when associated with congenital heart disease or induced by drug administration. The real incidence of pulmonary hypertension is difficult to evaluate and there are no treatments available to cure or halt its progression. Diagnosis of PH is very delicate, because preliminary symptoms, such as chest pain and shortness of breath, are not very specific. Because of the increase in RV pressure, the RV volume increases, affecting the pumping function on the right side but, at least in the initial phase of the condition, the left ventricle volume and ejection fraction remain normal. As the condition worsens, RV size increases and its shape becomes rounder, and the LV cavity is compressed.

Quantification of ventricular volume from standard 2-D echocardiography is commonly performed *via* planar measurements and use of a geometric model for volume estimation. This method is routinely applied in clinical practice for assessment of LV volume and ejection fraction. The left ventricle has an ellipsoidal shape with strong symmetry along a central axis, which allows volume estimation from 2-D echocardiographic images using geometrical models. On the other hand, the right ventricle is crescent-shaped and does not follow an axis of symmetry. For this reason, RV volume cannot be estimated from planar views and its function is not well-quantified during echocardiographic examination. In such situations, screening with RT3-D US appears to be critical for early diagnosis and accurate assessment of the severity of the pathology.

Study protocol

To test this hypothesis, we compared LV and RV volume and ejection fraction measures with RT3-D US and MRI for 10 volunteering patients with pulmonary hypertension (Institutional Review Board (IRB) protocol and signed agreements were obtained for this study). The set of patients included seven females and three males,

ages ranging from 6 to 63 y (median was 33 y). All patients had pulmonary arterial hypertension. Of these 8 had primary pulmonary hypertension and 2 had secondary pulmonary hypertension associated with congenital defects (1 with multiple ventricular septal defects closed at nine and 24 months of age and 1 with a sinus venosus defect). MRI data were acquired either before or after the echocardiographic examination. Manual tracing was performed on each modality by two cardiologists, "blinded" from each other's results. Typical RT3-D volumes were acquired in spherical coordinates with an angular field of view of 60° in azimuth and elevation and a slice thickness of 0.308 mm. Volumes were interpolated into a Cartesian coordinate system with voxel size of 0.6 mm^3 for segmentation. Between 10 to 17 volumes were acquired per cardiac cycle. Separate data sets were acquired for quantification of LV and RV function.

Manual tracing on RT3-D data

An expert cardiologist manually traced endocardial contours on selected slices and computed ventricular volumes *via* sector plane-disks summation using a dedicated software package from 3Dechotech©. Manual tracing was performed on the unprocessed data (*i.e.,* without denoising).

Manual tracing on MRI data

The MRI data were acquired with a 1.5 T GE clinical scanner using a fast cine sequence. There were two series of acquisition with acquisition parameters reported here: there were non-breath-hold, 8 mm slice thickness, 0 skip, 16 frames per beat, (36 mm × 36 mm) FOV, matrix 128 × 256 and breath hold, 8 mm slice thickness, 0 skip, 20 frames per beat (40 mm × 40 mm) FOV, matrix 128 × 256. An expert radiologist manually segmented the entire set of two-chamber views acquired for each patient with the Mass© v.5 software package (MEDIS Medical Imaging Systems, Inc, Leiden, The Netherlands) installed in the Department of Radiology at Columbia-Presbyterian Medical Center. End diastole and end systole volume were manually identified. Ventricular volumes were computed by adding slice areas, without using geometrical models.

For the two modalities, trabeculations and papillary muscles were excluded, but moderator bands were included inside the cavity.

Three-dimensional deformable model segmentation

Three-dimensional deformable-model segmentation was performed on the denoised data. The deformable model was initialized as a cone with ellipsoidal cross-section. The center and dimension of the ellipses were set up manually at the base, the apex and on the middle slice between the base and the apex of the ventricle. The ellipse dimensions were defined to reflect the ratio of dimensions of the ventricle, but the ellipse itself did not need to be close to the borders of the ventricle. We observed that using an ellipsoidal cross-section instead of a circle improved the stability and convergence of the iterative process. The cylinder height was defined from the base through 20 slices before the apex location, defined manually during the initialization process. By not including the apex, we let the model deform in the third dimension from slices above that have better resolution and we avoided problems of instability and oversegmentation.

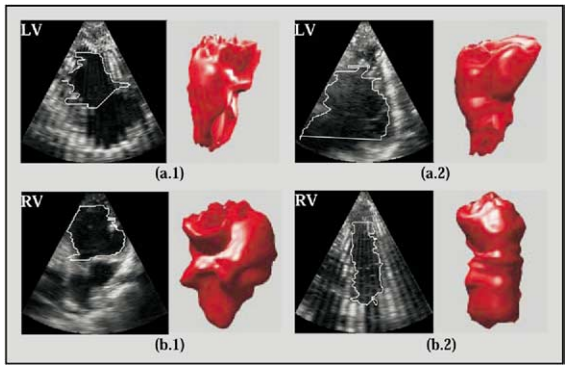

Fig. 2. LV and RV segmentation with deformable model performed on denoised RT3-D US for two patients (1 and 2) at end diastole. 3-D volumes are displayed with apex at bottom; RT3-D slices displayed with apex at top of image.

We illustrate in Fig. 2 the variety of RV and LV shapes segmented for four long-axis slices, with their corresponding deformable model contours overlaid and the ventricle's volume reconstructed in 3-D.

The set of 10 patients used in this study presented great diversity in the data quality as well as in ventricular shapes and sizes, as illustrated in Fig. 2. Quality of the US data depended on the acoustic window of the patient and on the ability of the cardiologist to acquire a good view of the patient's heart that included the entire cavity. In several cases, acquisition parameters had to be adapted to increase the depth setting and the FOV, sacrificing for acquisition quality. Regarding the ventricular shape, because of the enlarged RV cavity, the left ventricle can become very small in some patients and its shape, very distorted. The deformable model was well adapted in such situations, because it could accommodate any shape convexity while ensuring continuity and smoothness of the contour.

Study results

Ventricular volume and ejection fraction measures on RT3-D US data were compared with measures per-

Table 1. Quantification of EDV, ESV and EF for the RV for the 10 cases with manual tracing or deformable model on RT3-D US data and manual tracing on MRI data

	Manual tracing			Deformable model			MRI		
RV	EDV (mL)	ESV (mL)	EF (%)	EDV (mL)	ESV (mL)	EF (%)	EDV (mL)	ESV (mL)	EF (%)
1	NA	NA	NA	161.31	140.13	13.1	311.5	263.4	15.4
2	78.0	50.8	34.9	66.00	48.83	26.0	123.0	87.1	29.2
3	94.9	53.0	44.1	113.90	53.17	53.3	148.7	72.0	51.6
4	168.8	119.1	29.4	268.13	217.36	18.9	252.5	206.8	18.1
5	92.1	68.9	28.3	117.97	75.61	35.9	132.7	71.5	46.1
6	126.2	89.9	28.8	142.46	111.47	21.7	193.1	141.6	26.7
7	103.2	81.2	21.3	132.36	92.74	29.9	153.6	104.1	32.2
8	250.6	191.3	23.7	132.66	102.15	23.0	295.8	269.0	9.1
9	163.3	127.5	21.9	241.94	195.61	19.1	278.3	218.2	21.6
10	97.0	63.8	34.2	104.29	65.23	37.5	124.1	72.3	41.7
Mean	130.5	93.9	29.6	148.1	110.2	27.8	201.3	150.6	29.2

formed *via* manual tracing on MRI, which was considered to be the method of reference. Measurements and errors are reported in Table 1, Table 2 and Table 3 for the 10 clinical cases.

The first US case in the series for quantification of the RV function was not traced by the expert echocardiographer, because of poor visual quality. We were still able to apply our deformable model segmentation and to compare with MRI measurement.

Average measurements for EDV, ESV and EF showed that:

- RV volumes were larger than LV volumes, with all methods, consequence of the PH pathology
- EF was smaller for the RV, with all methods, also a consequence of the PH pathology
- Volume measurements provided larger values on MRI than on RT3-D, with a very different range of values
- Despite different ranges of volume values, average EF measurements were very similar with the three segmentation methods on MRI and RT3-D.

A similar phenomenon of overestimation of ventricular volumes with MRI was observed in a related study by Schmidt et al. (1999) focusing on LV measurement with RT3-D US.

To assess the effect of ventricular sizes and shapes on volumes and EF, we computed absolute errors of measurement for EDV, ESV and EF. We evaluated mean-error values and standard deviation (SD) over the 10 cases for the two ventricles. These error measures are reported in Table 3. Maximum and minimum error values are provided better to assess the range of variability achieved by the different segmentation methods.

This table revealed:

- Large mean errors for volume measurements on RT3-D US, with larger errors for larger volumes
- Very large SDs of errors for volume measurements
- Lower mean error for EF measurements estimated with the deformable model rather than with manual tracing on RT3-D US

Table 2. Quantification of EDV, ESV and EF for the LV for the 10 cases with manual tracing or deformable model on RT3-D US data and manual tracing on MRI data

	Manual tracing			Deformable model			MRI		
LV	EDV (mL)	ESV (mL)	EF (%)	EDV (mL)	ESV (mL)	EF (%)	EDV (mL)	ESV (mL)	EF (%)
1	44.4	19.3	56.1	30.87	15.75	49.0	79.0	37.2	52.9
2	59.1	35.0	40.8	56.30	23.92	57.5	41.4	19.0	54.0
3	96.5	49.2	49.0	94.90	53.00	44.1	127.6	48.0	62.4
4	53.3	28.0	47.5	84.97	32.70	61.5	61.0	24.8	59.2
5	77.7	34.1	56.1	131.03	39.84	65.6	144.8	36.9	74.5
6	40.4	12.9	68.1	59.86	23.62	60.5	70.0	27.7	60.4
7	35.8	11.8	67.0	48.44	18.77	61.2	47.6	19.0	60.0
8	67.3	38.1	43.4	128.44	91.16	29.0	118.0	82.2	30.4
9	78.5	39.8	49.3	70.22	40.75	42.0	141.3	76.2	46.1
10	64.0	31.3	51.1	73.03	26.38	63.9	65.8	21.2	67.8
Mean	61.7	30.0	52.8	77.8	36.6	53.4	89.7	39.2	56.8

Table 3. Absolute errors in quantification of EDV, ESV and EF on the 10 cases

	Manual vs. MRI			3-D Deformable model vs. MRI		
Error	EDV (mL)	ESV (mL)	EF (%)	EDV (mL)	ESV (mL)	EF (%)
RV, Mean	58.6	44.1	8.6	56.4	43.3	4.6
SD	26.6	34.3	5.6	54.8	55.6	4.2
Max	115.0	90.7	17.8	163.1	166.9	13.9
Min	27.1	2.6	0.3	14.7	4.1	0.8
LV, Mean	31.5	15.4	10.8	23.3	9.6	4.8
SD	22.7	14.4	5.3	21.7	10.7	5.3
Max	67.1	44.1	18.4	71.1	35.5	18.3
Min	1.8	1.2	3.2	0.8	0.2	0.1

Mean error (Mean), standard deviation (SD), maximum and minimum error values (Max-Min) are reported.

- Mean error for EF measurements similar for RV and LV
- SDs of errors for EF measurements were stable, similar for RV and LV and similar for manual tracing and deformable model.

These errors suggest that EF measurements are insensitive to the ventricular size and shape, which is not the case for volume measurements.

Further to apprehend the relative importance of the error values vs. the amplitude of the measure, we computed the mean percentage error of measurements on RT3-D US, as reported in Table 4

We also reported, in this table, results for RV for all the 10 cases and for nine cases, removing patient #8 with very suspicious volume measurements on MR, leading to an abnormally low EF of 9%. Without this patient, mean percentage EF errors dropped by 10%, while mean percentage volume errors remained similar. Overall, this table revealed that:

- Measurement errors had a relative proportion that depended more on the segmentation method than on the shape or size of the ventricle (*i.e.,* RV or LV and EDV or ESV)
- Error proportions were between 20% and 40% for volume measurements with both segmentation methods
- Error proportions for EF measurements were clearly lower with the deformable model, with an accuracy around 10% (not including patient #8 for the RV).

Even though manual tracing was performed using the same anatomical definition of the ventricular cavity, we can identify three potential sources of error to explain the discrepancy of volume measurements between RT3-D and MRI.

1. Regarding the imaging modalities, MRI image quality is far superior to that of US, but its spatial resolution is 26 times lower in the long axis dimension, leading to partial volume effect and slice overlapping. These artefacts lead to overestimation of ventricular volumes and are more important with larger ventricular cavities, acquired with lower axial resolution. We indeed observed larger volume measurement errors (*i.e.,* larger discrepancies of measurements and higher volume measurements with MRI) for the RV, with larger volumes. Higher quantification errors for bigger volumes were also reported in a similar study using RT3-D US (Corsi et al. 2001).
2. Regarding measurement methods, manual tracing on RT3-D US was performed on long-axis views of the original data by one cardiologist. A second cardiologist selected planes at the apex and the base of the heart on denoised long-axis views for segmentation with the deformable model. A third cardiologist performed manual tracing on the MRI data. The involvement of three cardiologists with differing expertise brings inherent variability into the manual measurements. Intra- and interobserver variabilities reported in previous clinical studies for RT3-D US were 2.4%

Table 4. Mean percentage error in quantification of EDV, ESV and EF for the 10 cases

	Manual vs. MRI			3-D Deformable model vs. MRI		
Mean error (%)	EDV	ESV	EF	EDV	ESV	EF
RV	31.4	28.3	39.6	25.9	24.2	25.6
RV (1 out)	33.4	28.2	24.5	22.7	20.0	11.5
LV	31.2	39.6	19.5	25.8	23.2	8.3

(intra) and 3.9% (inter) for LV EF (Takuma et al. 2001), 6 ± 17 mL (intra) and 3 ± 15 mL (inter) for LV volumes (Schmidt et al. 1999), 4% (inter) for RV volumes (Vogel et al. 1997). For MRI, values previously reported were around 8% (inter) for LV volumes (Apfel et al. 1996). These variability measures are typically computed as average absolute difference of measures expressed as a percentage or as two SDs of relative measure difference. It is therefore difficult to compare directly these values with average absolute error measures reported in this study. But, it is safe to presume that, according to the reported variability, an average error of EF measurements of around 10% is a reasonable lower bound for optimal errors of measurements from RT3-D US data, comparing with MRI. To put these results in perspective with other 3-D US modalities, a recent study (Mannaerts et al. 2003), using freehand 3-D US, reported intraobserver variability of measure around 6% for LV EF and percentual bias of measurements, when comparing with MRI of around 10%.

3. Finally, because of the enlarged right ventricular cavity, RT3-D data provided truncated volumes for some patients with severe disease, leading to unavoidable underestimation for volumes measured with US data. Truncation was limited to small regions near the apex, enclosing a very small volume of blood, rather constant through the cardiac cycle. EF measurements are rather insensitive to such small systematic volume underestimations.

Taking into account the limitations in the experimental protocol, as well as results commented on in the previous tables, we have focused our discussion on the statistical significance of the results on EF, less sensitive to all the potential sources of measurement errors, especially from MRI.

DISCUSSION

Correlation between ejection fraction measurements

To assess the agreement between the different methods, we first performed a linear regression and evaluated the correlation between the segmentation methods, along with assessment of the statistical significance of the correlation measure. The regression lines and correlation coefficients for RV and LV EF measurements are displayed in Fig. 3. The p value statistics for the correlation coefficients were evaluated as the probability of getting the measured correlation by random chance, in the hypothesis of zero correlation. Regression equations and p values were:

For manual tracing:
LV: $y = 0.31 \times x + 35.21$, $p = 0.23$

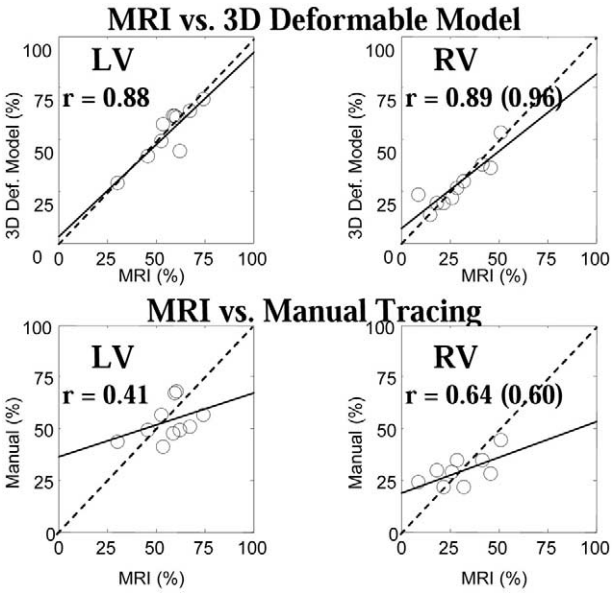

Fig. 3. Linear regression for RV and LV EF measures estimated with manual tracing on MRI, manual tracing on RT3-D US and deformable model on RT3-D US. Correlation coefficients are reported for each case. For the RV, correlation coefficients without patient #8 are reported inside the parentheses.

RV: $y = 0.34 \times x + 19.20$, $p = 0.06$
RV (not patient #8): $y = 0.37 \times x + 17.90$, $p = 0.11$

For the deformable model:
LV: $y = 0.90 \times x + 2.92$, $p = 8.810^{-4}$
RV: $y = 0.76 \times x + 5.77$, $p = 5.010^{-4}$
RV (not patient #8): $y = 0.94 \times x - 1.04$, $p = 3.3410^{-5}$

We observed higher correlation and linear regression fit closer to the identity line with the deformable model than with manual tracing. Measures for the RV were not significant (compared with a reference level of $p = 0.05$), but measures for the LV were. Good agreement *via* linear regression, high correlation coefficients with statistical significance, confirmed the high performance of the deformable model to segment the ventricular volumes on denoised RT3-D data for EF quantification.

Similar clinical studies have been reported recently in the literature. As mentioned in the introduction, Corsi et al. (2001, 2002), performed two studies comparing LV volumes and EF measurements from MRI and 3-D level-set segmentation on RT3-D data. In the first study (Corsi et al. 2001), they reported a correlation coefficient for LV volume measurements of r = 0.98 between manual tracing on MRI and level-set on RT3-D (computed on a "small" number of cases, according to the authors) from a data base of 21 healthy or diseased patients. No significance levels were reported. In a second study by Corsi et al. 2002, this group used the same level-set segmentation method and reported a correlation coeffi-

cient for LV EF measurement of r = 0.87 between level-set on RT3-D US and manual tracing on MRI data for a group of nine patients out of a database of 21 patients with ischemia or dilated cardiomyopathy. This correlation ratio is similar to the ones reported by our study, but no significance levels were reported in their case. It is very difficult to compare these studies with ours because, they report very few results for EF measurements with manual tracing on MRI. It seems that performance of the level-set segmentations is comparable with very accurate EF measurements. We point out here that the level-set energy functional used by this group relies on gradient information, constraining the initialization to be close to the endocardial border, which is not the case with our algorithm. Schmidt et al. (1999) performed a study on 14 patients for LV volume measurement *via* manual tracing on MRI and RT3-D US. They reported correlation factors of r = 0.88 for LV EDV, r = 0.82 for LV ESV and r = 0.72 for LV EF, with $p < 0.001$ for both EDV and ESV. Lee et al. (2001) performed a similar study on 25 patients and reported correlation factors of between 0.92 and 0.99 for volumes and EF with significance level $p < 0.05$. Mondelli et al. (2001) performed a study on 18 patients for LV EF measurement *via* manual tracing on RT3-D US compared with MUGA, and reported a correlation r = 0.94 for LV EF. In a similar study on 43 patients, Takuma et al. (2001) reported a correlation r = 0.9 for LV EF, with no significant difference between the identity line and the linear regression (F test). For RV segmentation, Shiota et al. (1998) performed a study for quantification of RV volume on six sheep *via* manual tracing on RT3-D US and reported a correlation of r = 0.87 with $p < 0.001$. Compared with these results, our study reported similar correlation coefficients for RV and LV EF measures, with statistical significance ($p < 0.001$). Regarding inter and intraobserver variabilities for manual tracing on RT3-D US, the clinical study from Takuma et al. (2001) reported an interobserver variability equal to 2.4% and an intraobserver variability equal to 3.9% and no significant difference in EF measurements made on RT3-D US and on MUGA. The same manual tracing method was used in our study and we can use this result as a reference and state that relative absolute error of measurements of 10% reflects a good performance of the deformable model segmentation for EF measurements on RT3-D US.

Bland–Altman error analysis for ejection fraction measurements

For further evaluation, we performed a Bland–Altman statistical analysis (Bland and Altman 1986). We considered measures from MRI data as the reference (ground truth) and computed errors of RT3-D measures vs. MRI, as in Vogel et al. (1997) and Shiota et al. (1998), with either manual tracing or the deformable model. Results of the Bland–Altman analysis are displayed in Fig. 4.

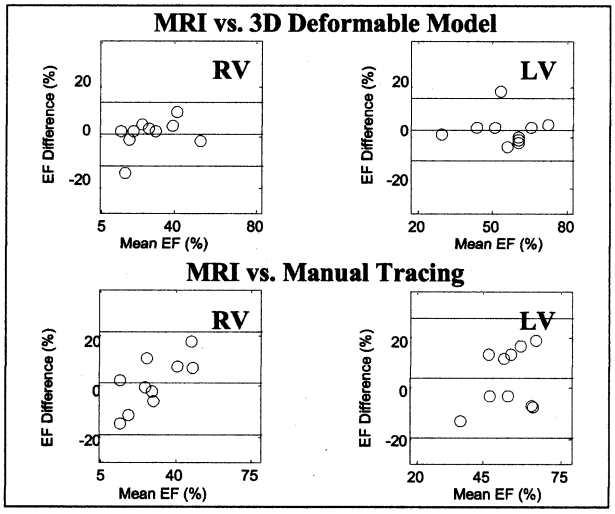

Fig. 4. Bland–Altman statistical analysis for LV and RV EF measures with manual tracing and 3-D deformable model on RT3-D US vs. manual tracing on MRI. Average EF difference and 95% confidence interval are displayed on each plot.

The 95% confidence interval is defined with a center value equal to the mean error and width equal to two SDs of the error.

These error intervals were equal to:

3-D deformable model on RT3-D ultrasound 1.31% ± 6.27% for RV EF and 2.93% ± 6.13% for LV EF

Manual tracing on RT3-D US 1.20% ± 10.09% for RV EF and 3.93% ± 11.80% for LV EF.

Analysis of the errors showed that the 3-D deformable model applied to denoised RT3-D US performed as accurately as manual tracing, while reducing the mean error and the confidence interval by up to 37% for RV EF and 48% for LV EF.

Schmidt et al. (1999) reported, in their study for quantification of LV volumes, a mean error of 16 mL ± 36 mL when combining ESV and EDV estimations, with an intraobserver variability of 6 mL ± 17 mL and an interobserver variability of 3 mL ± 15 mL. Corsi et al. (2001) reported a confidence interval equal to 0.42 mL ± 5.78 mL for LV volume measurement, comparing manual tracing and 3-D level-set segmentation on RT3-D data. Takuma et al. (2001) reported standard error of estimate of 4% for LV EF measures, when compared with MUGA. They also reported interobserver variability of 2.4%–3.7% and intraobserver variability of 3.9%–8.3%, for two different manual tracing methods.

Regarding RV function, Ota et al. (1999) reported, in a study for *in vitro* and *in vivo* RV volume measure-

ment with RT3-D US, a standard error of estimate of 3.26 mL *in vitro,* and 8.1 mL *in vivo.* This study also reported an interobserver variability of 4.1 mL (8.3% of the mean) for ESV, 7.2 mL (9.4% of the mean) for EDV and 2.4 mL (8.1% of the mean) for stroke volume measurement *via* manual tracing on RT3-D US data. As the authors pointed out in their conclusion, this study showed that *in vivo* RV volume measurement with RT3-D US was feasible, but did not validate their measurements for EDV and ESV. A study on LV measures for PH patients with 3-D echocardiography reported an interobserver variability of 8.3% and 7.6% for ESV and EDV (Apfel et al. 1996).

In conclusion, analysis of measurements on RT3-D US showed that:

- Quantification of ventricular volume is still problematic on RT3-D US. Errors of measurement, comparing with MRI, were large, increased with volume size and showed high variability.
- Quantification of EF with RT3-D US is insensitive to volume size and produced similar mean errors with manual tracing and deformable model.
- Deformable model provided EF measurements with higher correlation (with statistical significance), better linear regression and lower variability than manual tracing, comparing with MRI.
- For EF measurements, an average absolute error of 5% and a relative average absolute error of 10% were achieved with the deformable model.

We can conclude that quantification of cardiac function with RT3-D US, *via* deformable model segmentation on denoised data, is feasible and provides accurate ejection fraction measures, compared with MRI. Manual tracing measures were less reliable with large SD of errors and low correlation coefficients.

SUMMARY

The long-term goal of this research project was to design and validate a method of dynamic analysis for recently- developed RT3-D US technology that would provide cardiologists with a new portable, low cost, easy to administer and non-invasive diagnostic instrument. The design of such analysis tools for 3-D US is crucial since all other existing 3-D protocols available for dynamic cardiac screening, which include high-speed CT, phase contrast MRI and tagged MRI, cannot compare with the flexibility and the ease of acquisition offered by US, limiting their application and use in routine and emergency clinical practice.

The challenge of developing a segmentation tool for quantification of cardiac function from RT3-D US lies in the novelty of the data themselves and the wealth of dynamic information that can be extracted, despite their low spatial resolution and high levels of speckle noise. We have implemented a 3-D deformable model level-set segmentation method. This deformable model was derived from the Mumford–Shah minimization method, deforming a surface to achieve an optimal partitioning of the data into homogeneous regions. This deformable model proved to be very well-suited for segmentation of RT3-D US as it extracted highly curved volumes while ensuring smoothness to handle missing myocardium signals and inside localized echo signals from trabeculations.

We presented a clinical study on the validation of volume quantification using RT3-D US, focusing on 10 PH patients for RV and LV volume quantification with MRI screening available as the "reference." This clinical study reported high correlation for ejection fraction, with good statistical significance. Experiments on clinical RT3-D data have shown that we can extract LV and RV contours using a 3-D deformable model and quantify volumes of interest with a higher degree of accuracy than achieved with manual tracing. Errors of measurement for ejection fraction were within the range of inter- and intraobserver variability reported by our collaborators from the Echocardiography Laboratories. These errors also compared favorably with similar studies performed by other groups using RT3-D US for quantification of cardiac function.

Future applications applying dynamic segmentation to real-time 3-D US include stress-echo testing and endocardial wall motion analysis, which can provide quantitative estimates of ischemic myocardial tissue locations and extent. Significant efforts have been carried out to characterize myocardial wall deformation with cine MR imaging and MR tagging, but their application is limited by cost factors and difficulty in screening ill patients with the MR modality. Echocardiography appears again as the modality of choice for the analysis of wall motion, if suitable segmentation and analysis tools can be developed for 3-D US technology. A recent study using a 3-D rotational transducer on open-chest dogs (Papademetris et al. 2001) demonstrated the feasibility of quantitative analysis of LV myocardium walls with echocardiography images and will be a focus of our future work in this direction. We have presented some preliminary work in that direction using finite element meshes and parameterization of the endocardial geometry in Angelini et al. (2002).

Clinical use of RT3-D transducers has not been fully realized in terms of both data visualization and the extraction of quantitative information, since no tools are available to perform these tasks in a completely automated fashion. Some commercial software tools are now available for assisted manual tracing. The long-term goal

of this project aimed to advance this state-of-the-art new US technology by developing a dynamic denoising and segmentation tool that will improve temporal 3-D visualization of the myocardium and compute physiological parameters for assessment of cardiac function. Parallel efforts are continuously underway to improve the technology of real-time 3-D US transducers (Inerfield et al. 2002; Yen and Smith 2002), by increasing spatial resolution and reducing hardware noise and artefacts. A new generation of RT3-D transducer was recently commercialized by Philips Medical System with the iE33 system.

ACKNOWLEDGEMENTS

The authors thank Dr. Gersony and Dr. Donis from the Echocardiography Laboratories at the Columbia University Medical Center for their participation in this project. This project was funded by the American Heart Association (grant 0151250T).

REFERENCES

Amadieu O, Debreuve E, Barlaud M, Aubert G. Inward and outward curve evolution using level set method. International Conference on Image Processing, Kobe, Japan. 1999:188–192.

Angelini E, Laine A, Takuma S, Holmes J, Homma S. LV volume quantification via spatio-temporal analysis of real-time 3D echocardiography. IEEE Trans Med Imaging 2001;20(6)457–469.

Angelini ED, Laine A. Spatio-temporal directional analysis of real-time three dimensional cardiac ultrasound. In: Petrosion A, Meyer F, eds. Wavelets in signal and image analysis. From theory to practice. Dordrecht, Boston, London: Kluwer Academic Publishers, 2001: 379–416.

Angelini ED, Hamming D, Homma S, Holmes J, Laine A. Comparison of segmentation methods for analysis of endocardial wall motion with real-time three-dimensional ultrasound. Comput Cardiol 2002; 609–612.

Angelini ED, Holmes J, Laine AF, Homma S. Segmentation of real-time 3D cardiac ultrasound with implicit deformable models without gradients. International Symposium on Image and Signal Processing and Analysis, Rome, Italy. 2003;711–716.

Apfel HD, Shen Z, Gopal AS, et al. Quantitative three dimensional echocardiography in patients with pulmonary hypertension and compressed left ventricles: Comparison with cross sectional echocardiography and magnetic resonance imaging. Heart 1996;76(4): 350–354.

Ashton EA, Parker KJ. Multiple resolution Bayesian segmentation of ultrasound images. Ultraso Imaging 1995;17(4):291–304.

Aubert G, Vese L. A variational method in image recovery. SIAM J Numerical Anal 1997;34(5):1948–1979.

Belohlavek M, Foley DA, Gerber TC, et al. Three- and four-dimensional cardiovascular ultrasound imaging: A new era for echocardiography. Mayo Clin Proc 1993;68(3):221–240.

Bland JM, Altman DG. Statistical methods for assessing agreement between two methods of clinical measurements. Lancet 1986;1: 307–310.

Boukerroui D, Basset O, Baskurt A, Noble A. Segmentation of echocardiographic data. Multiresolution 2D and 3D algorithm based on grey level statistics Cambridge, UK: MICCAI. 1999:516–523.

Chalana V, Linker DT, Haynor DR, Kim Y. A multiple active contour model for cardiac boundary detection on echocardiographic sequences. IEEE Trans Med Imaging 1996;15(3):290–298.

Chan TF, Vese LA. Active contours without edges. IEEE Trans Image Proc 2001;10(2):266–277.

Chen Y, Thiruvenkadam S, Tagare HD, et al. On the incorporation of shape priors into geometric active contours. IEEE Workshop on Variational and Level Set Methods in Computer Vision, Vancouver, BC, Canada. 2001;145–152.

Chen Y, Huang F, Tagare HD, et al. Using prior shape and intensity profile in medical image segmentation. IEEE International Conference on Computer Vision (ICCV), Nice, France. 2003;1117–1124.

Cohen LD, Cohen I. Finite-elements methods for active contour models and balloons for 2- D and 3-D Images. IEEE Trans Pattern Anal Machine Intell 1993;15 (11):1131–1147.

Coppini G, Poli R, Valli G. Recovery of the 3-D shape of the left ventricle from echocardiographic images. IEEE Trans Med Imaging 1995;14(2):301–317.

Corsi C, Borsari M, Consegnati F, et al. Left ventricular endocardial surface detection based on real-time 3D echocardiographic data. Eur J Ultrasound 2001;13(1):41–51.

Corsi C, Saracino G, Sarti A, Lamberti C. Left ventricular volume estimation for real-time three-dimensional echocardiography. IEEE Trans Med Imaging 2002;21(9):1202–1208.

Cremers D, Schnorr C, Weickert J. Diffusion-snakes: combining statistical shape knowledge and image information in a variational framework. Workshop on Variational and Level Set Methods in Computer Vision, Vancouver, BC, Canada. 2001;137–144.

Detmer PR, Bashein G, Martin RW. Matched filter identification of left-ventricular endocardial borders in transoesophageal echocardiograms. IEEE Trans Med Imaging 1990;9(4):396–404.

Dias JMB, Leitao JMN. Wall position and thickness estimation from sequences of echocardiographic images. IEEE Trans Med Imaging 1996;15(1):25–38.

Drezek R, Stetten GD, Ota T, et al. Active contour based on the elliptical Fourier series, applied to matrix-array ultrasound of the heart. AIPR Workshop: Emerging Applications of Computer Vision. 1997;26–34.

Feng J, Lin W, Chen C. Epicardial boundary detection using fuzzy reasoning. IEEE Trans Med Imaging 1991;10(2):187–199.

Fenster A and Downey DB. Three-Dimensional Ultrasound Imaging. In: Beutel ALJK, Metter RL, eds. Handbook of Medical Imaging. Vol. 1. Physics and Psychophysics. Bellingham, WA: SPIE, 2000: 463–510.

Fenster A, Downey DB, Cardinal HN. Three-dimensional ultrasound imaging. Phys Med Biol 2001;46(5):R67–R99.

Friedland N, Adam D. Automatic ventricular cavity boundary detection from sequential ultrasound images using simulated annealing. IEEE Trans Med Imaging 1989;8(4):344–353.

Herlin I, Bereziat D, Giraudon G, Nguyen C, Graffigne C. Segmentation of echocardiographic images with Markov random fields. European Conference on Computer Vision. Stockholm, Sweden: Springer. 1994;201–206.

Herlin LL and Giraudon G. Performing segmentation of ultrasound images using temporal information. International Conference on Computer Vision and Pattern Recognition, New York, NY, USA. 1993:373–378.

Hunter IA, Soraghan JJ, McDonagh T. Fully automatic left ventricular boundary detection in echocardiographical images. Comput Cardiol 1995;741–744.

Inerfield M, Lockwood GR, Garverick SL. A sigma-delta-based sparse synthetic aperture bcamformer for real-time 3-D ultrasound. IEEE Trans Ultrason Ferroelec Freq Control 2002;49(2):243–254.

Jones TN, Metaxas DN. Automated 3D segmentation using deformable models and fuzzy affinity. Duncan JS, Gindi G, eds. 15th International Conference, Information Processing in Medical Imaging, Vermont, Springer: USA. 1997;113–126.

Kao C-M, Pan X, Hiller E, Chen C-T. A Bayesian approach for edge detection in medical ultrasound images. IEEE Trans Nuclear Sci 1998;45(6):3089–3096.

Kass M, Witkin A, Terzopoulos D. Snakes: Active contour models. Int J Comput Vision 1987;1:321–331.

Kimmel R, Malladi R, Sochen N. Images as embedded maps and minimal surfaces: movies, color, texture, and volumetric medical images. Int J Comput Vision 2000;39(2):111–129.

Kisslo J, Firek B, Ota T, et al. Real-time volumetric echocardiography: The technology and the possibilities. Echocardiography 2000;17(8):773–779.

Klingler JW, Vaughan CL, Fraker TD, Andrews LT. Segmentation of echocardiographic data using mathematical morphology. IEEE Trans Biomed Eng 1988;35:925–934.

Lee D, Fuisz A, Fan P-H, et al. Real-time 3-dimensional echocardiographic evaluation of left ventricular volume: Correlation with magnetic resonance imaging—A validation study. J Am Soc Echocardiog 2001;14(10):1001–1009.

Lin N, Yu W, Duncan JS. Combinative multi-scale level set framework for echocardiographic image segmentation. Med Image Anal 2003; 7(4):529–537.

Loncaric S, Subasic M, Sorantin E. 3-D deformable model for aortic aneurysm segmentation from CT images. International Conference of the IEEE Engineering in Medicine and Biology Society, Chicago, IL, USA. 2000;398–401.

Lotjonen J, Magnin IE, Reissman P-J, Nenomen J, Katilla T. Segmentation of magnetic resonance images using 3D deformable models. In: Wells WM III, Colchester ACF, Delp S, eds. Medical image computing and computer-assisted intervention. Boston, MA: Springer, 1998:1213–1221.

Malassiotis S, Strintzis MG. Tracking the left ventricle in echocardiographic images by learning heart dynamics. IEEE Trans Med Imaging 1999;18(3):282–290.

Malladi R and Sethian JA. Level set and fast marching methods in image processing and computer vision. IEEE International Conference on Image Processing, Lausanne, Switzerland. 1996:489–492.

Malladi R, Kimmel R, Adalsteinsson D, et al. A geometric approach to segmentation and analysis of 3D medical images. Workshop on Mathematical Methods in Biomedical Image Analysis. 1996:244–252.

Malladi R, Sethian JA, Vemuri BC. Shape modeling with front propagation: A level set approach. IEEE Trans Pattern Anal Machine Intell 1995;17(2):158–175.

Mannaerts HF, Heide JAVD, Kamp O, et al. Quantification of left ventricular volumes and ejection fraction using freehand transthoracic three-dimensional echocardiography: Comparison with magnetic resonance imaging. J Am Soc Echocardiog 2003;16(2):101–109.

Metaxas DN. Physics-based deformable models. Applications to computer vision, graphics and medical imaging, 1997.

Meyer F, Coifman RR. Brushlets: A tool for directional image analysis and image compression. App Computat Harmonic Anal 1997;4(1): 147–187.

Mikic I, Kruncinski S, Thomas JD. Segmentation and tracking in echocardiographic sequences: Active contour guided by optical flow estimates. IEEE Trans Med Imaging 1998;17(2):274–284.

Mondelli JA, Luzio SD, Nagaraj A, et al. The validation of volumetric real-time 3-dimensional echocardiography for the determination of left ventricular function. J Am Soc Echocardiog 2001;14(10):994–1000.

Montagnat J, Delingette H, Ayache N. A review of deformable surfaces: Topology, geometry and deformation. Image Vision Comput 2001;19(14):1023–1040.

Montagnat J, Delingette H, Scape N, and Ayache N. Surface simplex meshes for 3D medical image segmentation. IEEE International Conference on Robotics and Automation. 2000:864–870.

Morel J-M, Solimini S. Variational methods in image segmentation. Boston: Birkhauser, 1994.

Morsy AA, Stetten GD, Von Ramm OT. Detection and quantification of true 3D motion components of the myocardium using 3D speckle tracking in volumetric ultrasound scans: Simulations and initial experimental results. SPIE Conference on Medical Imaging: Physiology and Function from Multidimensional Images. Hoffman EA ed. SPIE. 1997;346–353.

Mumford D, Shah J. Boundary detection by minimizing functional. International Conference on Computer Vision and Pattern Recognition, San Francisco, CA, USA. 1985;22–26.

Ofili EO, Nanda NC. Three-dimensional and four-dimensional echocardiography. Ultrasound Med Biol 1994;20:669–675.

Osher S, Sethian JA. Fronts propagating with curvature-dependent speed: Algorithms based on Hamilton–Jacobi formulations. J Comput Phys 1988;79(1):12–49.

Ota T, Fleishman CE, Ohazama CJ, et al. Measurement of left ventricular volume by real-time, three-dimensional echocardiography in dogs. Circulation (Suppl) 1990;94(1):379.

Ota T, Fleishman CE, Strub M, et al. Real-time, three-dimensional echocardiography: Feasibility of dynamic right ventricular volume measurement with saline contrast. Am Heart J 1999; 137(5):958–966.

Papademetris X, Sinusas AJ, Dione DP, Duncan JS. Estimation of 3D left ventricular deformation from echocardiography. Med Image Anal 2001;5(1):17–28.

Papadopoulos I and Strintzis MG. Bayesian contour estimation of the left ventricle in ultrasound images of the heart. International Conference of the IEEE Engineering in Medicine and Biology Society, Montreal, Canada. 1995.

Paragios N. A level set approach for shape-driven segmentation and tracking of the left ventricle. IEEE Trans Med Imaging 2003;22(6): 773–776.

Paragios N, Deriche R. Geodesic active contours and level sets for the detection and tracking of moving objects. IEEE Trans Pattern Anal Machine Intell 2000;22(3):266–280.

Ramm OTV, Smith SW. Real time volumetric ultrasound imaging system. J Digital Imaging 1990;3(4):261–266.

Rankin RN, Fenster A, Downey DB, et al. Three-dimensional sonographic reconstruction: Technique and diagnostic applications. Am J Radiol 1993;161:695–702.

Rudin LI, Osher S, Fatemi E. Nonlinear total variation based noise removal algorithms. Physica D 1992;60:259–268.

Sarti A, Malladi R, Sethian JA. Subjective surfaces: a geometric model for boundary completion. International Journal of Computer Vision 2002;46(3):201–221.

Schmidt MA, Ohazama JC, Agyeman KO, et al. Real-time three-dimensional echocardiography for measurement of left ventricular volumes. Am J Cardiol 1999;84(12):1434–1439.

Setarehdan SK, Soraghan JJ. Fuzzy multiscale edge detection (FMED) applied to automatic left ventricle boundary extraction. 7th International Conference on Image Processing and its Applications, Manchester, UK. 1999;552–556.

Sethian JA. Theory, algorithms, and applications of level set methods for propagating surfaces. Acta Numerica 1996:309–395.

Sethian JA. Level set methods and fast marching methods: Evolving interfaces in computational geometry, fluid mechanics, computer vision, and materials science. Cambridge, UK: Cambridge University Press, 1999.

Shattuck DP, Weinshenker MD, Smith SW, Von Ramm OT. Exploroscan: A parallel processing technique for high speed ultrasound imaging with linear phased arrays. J Acoust Soc Am 1984;75(4): 1273–1282.

Shiota T, Jones M, Chikada M, et al. Real-time three dimensional echocardiography for determining right ventricular stroke volume in an animal model of chronic right ventricular volume overload. Circulation 1998;97(19):1897–1900.

Staib LH and Duncan JS. Left ventricular analysis from cardiac images using deformable models. Computers in Cardiology, Washington, DC. 1989;1:427–430.

Stetten G, Ota T, Ohazama C, et al. Real-time 3D ultrasound: A new look at the heart. J Cardiovasc Diagn Proc 1998;15(2):73–84.

Suri JS. Leaking prevention in fast level sets using fuzzy models: An application in MR brain. IEEE EMBS International Conference on Information Technology Applications in Biomedicine, Arlington, VA, USA. 2000;220–225.

Takuma S, Ota T, Muro T, et al. Assessment of left ventricular function by real-time 3D echocardiography compared with conventional noninvasive methods. J Am Soc Echocardiog 2001;14(4):275–284.

Thomas JG, II RAP, Jeanty P. Automatic segmentation of ultrasound images using morphological operators. IEEE Trans Med Imaging 1991;10(2):180–186.

Trobaugh JW, Arthur RM. Representation of shape in ultrasonic images with a physically-based image model. IEEE Workshop on Mathematical Methods in Biomedical Image Analysis. Kauai, HI, USA. 2001:79–86.

Tsai A, Yezzi A. Jr, Willsky AS. Curve evolution implementation of the Mumford-Shah functional for image segmentation, denoising, interpolation, and magnification. IEEE Trans Image Pro 2001; 10(8):1169–1186.

Vese LA, Chan TF. A multiphase level set framework for image segmentation using the Mumford and Shah model. Int J Comput Vision 2002;50(3):271–293.

Vogel M, Gutberlet M, Dittrich S, Hosten N, Lange PE. Comparison of transthoracic three dimensional echocardiography with magnetic resonance imaging in the assessment of right ventricular volume and mass. Heart 1997;78(2):127–130.

Wang X, Wee WG. A new deformable contour method. In: International Conference on Image Analysis and Processing, Venice, Italy: EURASIP. 1999;430–435.

Xiao G, Brady M, Noble JA, Zhang Y. Segmentation of ultrasound B-mode images with intensity inhomogeneity correction. IEEE Trans Med Imaging 2002;21(1):48–57.

Xiaolan Z, Staib LH, Schultz RT, Duncan JS. Segmentation and measurement of the cortex from 3-D MR images using coupled-surfaces propagation. IEEE Trans Med Imaging 1999;18(10):927–937.

Xin Y, Boekarerts P, Bister M, Taeymans Y, Cornelis J. Left ventricular boundary detection in echocardiographical images using artificial neural networks. European Conference on Signal Processing. 1992:1199–1202.

Yen JT, Smith SW. Real-time rectilinear volumetric imaging. IEEE Trans Ultrason Ferroelec Freq Control 2002;49(1):114–124.

Yezzi A Jr, Kichenassamy S, Kumar A, Olver P, Tannenbaum A. A geometric snake model for segmentation of medical imagery. IEEE Trans Med Imaging 1997;16 (2):199–209.

Zhao H-K, Chan T, Merriman B, Osher S. A variational level set approach to multiphase motion. J Comput Phys 1996;127(1):179–195.

APPENDIX

Dynamic implementation of the level-set deformable model

Computation of the Euler–Lagrange equation associated with the minimization of eqn (10) requires regularization of the Heaviside and Dirac functions as detailed in Chan and Vese (2001) and Zhao et al. (1996). In our implementation, we have chosen the regularization functions $H_\varepsilon(\phi)$ and $\delta_\varepsilon(\phi)$ proposed by Chan and Vese (2001), which are defined with ε a neighborhood parameter and have nonzero values everywhere.

$$H_\varepsilon(z) = \frac{1}{2}\left(1 + \frac{2}{\pi}\arctan\left(\frac{\pi z}{\varepsilon}\right)\right) \tag{14a}$$

$$\delta_\varepsilon(z) = \frac{dH(z)}{dz} = \frac{\varepsilon^2}{\varepsilon^2 + (\pi z)^2}. \tag{14b}$$

Both functions tend to the nonregularized definition of $H(z)$ and $\delta(z)$ as $\varepsilon \to 0$.

It can be shown, as in Vese and Chan (2002), that the approximation of the zero-level curve length from eqn (8), using the regularized Dirac function and defined as:

$$L_\varepsilon(\phi = 0) = \int_\Omega \delta_\varepsilon(\phi)\left|\nabla(\phi)\right| d\Omega \tag{15}$$

will converge to the exact length of the zero-level curve as ε tends to zero:

$$\lim_{\varepsilon \to 0} L_\varepsilon(\phi = 0) = \int_{\phi=0} ds = \left|C_0(s)\right|, \tag{16}$$

with $C_0(s)$ the zero-level curve with curvilinear parameter $0 \le s \le 1$. No issue is raised by the exact area approximation in eqn (9).

Derivation of the Euler–Lagrange equation is provided in Chan and Vese (2001) and is expressed as:

$$\begin{aligned} &\delta_\varepsilon(\phi)\left[\mu div\left(\frac{\nabla\phi}{\left|\nabla\phi\right|}\right) - \nu - \lambda_0(I - c_0)^2 + \lambda_1(I - c_1)^2\right] = 0 \; on \; \Omega \\ &\frac{\delta_\varepsilon(\phi)}{\left|\nabla\phi\right|}\frac{\partial\phi}{\partial n} = 0 \; on \; \partial\Omega, \end{aligned} \tag{17}$$

where $\frac{\partial}{\partial n}$ defines the partial derivative along the normal to the zero-level curve of ϕ. We observe here the introduction of the curvature of the zero-level front $K(\phi) = -div\left(\frac{\nabla\phi}{|\nabla\phi|}\right)$, as with the popular level-set algorithm for segmentation *via* motion under mean curvature introduced by Osher and Sethian (1988). The motion by mean curvature is driven by the following system:

$$\begin{cases} \dfrac{\partial\phi(x,t)}{\partial t} = \left|\nabla\phi(x,t)\right| div\left(\dfrac{\nabla\phi(x,t)}{\left|\nabla\phi(x,t)\right|}\right), \\ \phi(x,0) = \phi_0 \end{cases} \tag{18}$$

and the level curves of ϕ move by mean curvature in the normal direction.

DISCRETIZATION AND PARAMETERS VALUES

Implementation of the energy minimization problem is performed with a finite difference scheme for spatial derivatives and the introduction of an artificial time component to model the descent iteration. We denote by $\{\Delta x, \Delta y, \Delta z\}$ the spatial sampling units in the 3-D space, Δt the temporal increment unit and we evaluate the function $\phi(x, y, z, t)$ at node points (i, j, k) and time n.

Using an explicit scheme for the time derivative, the iterative process is:

$$\begin{aligned} \phi_{i,j,k}^{n+1} = \phi_{i,j,k}^n + \Delta t \times \delta_\varepsilon\left(\phi_{i,j,k}^n\right)\Bigg[&-\mu div\left(\frac{\nabla\phi_{i,j,k}^n}{\left|\nabla\phi_{i,j,k}^n\right|}\right) + \nu + \lambda_0\left(I_{i,j,k}\right. \\ &\left. - c_0(\phi^n)\right)^2 - \lambda_1\left(I_{i,j,k} - c_1(\phi^n)\right)^2\Bigg] \end{aligned} \tag{19}$$

with $\lambda_0 \ge 0$, $\lambda_1 \ge 0$, $\mu \ge 0$, $\nu \ge 0$. We point out here that the signs were modified from the implementation from Chan and Vese (2001), as we considered $\phi < 0$ inside the object to be consistent with the standard level set implementation in Malladi et al. (1995). We also had to modify the Heaviside function $H_\varepsilon(\phi)$ to have positive values for $\phi < 0$ as:

$$H_\varepsilon(z) = \frac{1}{2}\left(1 - \frac{2}{\pi}\arctan\left(\frac{\pi z}{\varepsilon}\right)\right), \tag{20}$$

while the Dirac function was kept positive.

We further modified the terms associated with the average values to better control their effect on the deformation process through λ_0 and λ_1 by normalizing as follows:

$$\begin{aligned} \phi_{i,j,k}^{n+1} = \phi_{i,j,k}^n + \Delta t * \delta_\varepsilon\left(\phi_{i,j,k}^n\right)\Bigg[&-\mu div\left(\frac{\nabla\phi_{i,j,k}^n}{\left|\nabla\phi_{i,j,k}^n\right|}\right) + \nu \\ &+ \lambda_0\frac{\left(I_{i,j,k} - c_0(\phi^n)\right)^2}{c_0(\phi^n)^2} - \lambda_1\frac{\left(I_{i,j,k} - c_1(\phi^n)\right)^2}{c_1(\phi^n)^2}\Bigg]. \end{aligned} \tag{21}$$

The curvature term was computed with the mean curvature model as:

$$\begin{aligned} div\left(\frac{\phi}{\left|\phi\right|}\right) = &\frac{\left(\phi_{yy} + \phi_{zz}\right)\phi_x^2 + \left(\phi_{xx} + \phi_{zz}\right)\phi_y^2 + \left(\phi_{xx} + \phi_{yy}\right)\phi_z^2}{\left(\phi_x^2 + \phi_y^2 + \phi_z^2\right)^{3/2}} \\ &- \frac{\left(2\phi_x\phi_y\phi_{xy} + 2\phi_x\phi_z\phi_{xz} + 2\phi_y\phi_z\phi_{yz}\right)}{\left(\phi_x^2 + \phi_y^2 + \phi_z^2\right)^{3/2}}. \end{aligned} \tag{22}$$

Following the initial approach of Malladi et al. (1995) for motion under mean curvature, the spatial derivatives are approximated with centered differences, as follows:

$$\phi_x^n(i\Delta x, j\Delta y, k\Delta z) = \frac{\phi_{i+1,j,k}^n - \phi_{i-1,j,k}^n}{2\Delta x} \tag{23a}$$

$$\phi_{xx}^n(i\Delta x, j\Delta y, k\Delta z) = \frac{\phi_{i+1,j,k}^n - 2\phi_{i,j,k}^n + \phi_{i-1,j,k}^n}{\Delta x^2} \tag{23b}$$

$$\phi_{xy}^n(i\Delta x, j\Delta y, k\Delta z) = \frac{\phi_{i+1,j+1,k}^n - 2\phi_{i,j,k}^n + \phi_{i-1,j-1,k}^n}{\Delta x \Delta y}, \tag{23c}$$

and similarly for the other derivatives $\phi_y, \phi_z^n, \phi_{yy}^n, \phi_{zz}^n, \phi_{xz}^n, \phi_{yz}^n$.

We point out here that Chan and Vese (2001) used a different curvature model initially proposed by Rudin et al. (1992), which combined both centered and one-sided spatial derivatives, but did not explicitly include cross derivatives. We also point out that Chan and Vese (2001) used a semi-implicit scheme for the curvature term to constrain bounds on ϕ^n and ϕ^{n+1} to be similar, as in Aubert and Vese (1997), and make the numerical scheme unconditionally stable. The unconditionally stable scheme allows for arbitrary time step values to speed up the iteration process. On the other hand, the semi-implicit scheme requires two updates of the function ϕ^{n+1} at each iteration, which can become problematic when manipulating large volumetric data sets.